Portland State University

PDXScholar

Civil and Environmental Engineering Faculty Publications and Presentations

Civil and Environmental Engineering

12-2013

Turbulent Kinetic Energy and Coherent Structures in a Tidal River

Stefan A. Talke
Portland State University, talke@pdx.edu

Alexander R. Horner-Devine
University of Washington - Seattle Campus

C. Chris Chickadel
University of Washington - Seattle Campus

Andrew T. Jessup
University of Washington - Seattle Campus

Follow this and additional works at: https://pdxscholar.library.pdx.edu/cengin_fac

Part of the Civil Engineering Commons, and the Environmental Engineering Commons

Let us know how access to this document benefits you.

Citation Details

Turbulent kinetic energy and coherent structures in a tidal river

S. A. Talke,[1] A. R. Horner-Devine,[2] C. C. Chickadel,[3] and A. T. Jessup[2,3]

[1] We investigate the relationship between turbulence statistics and coherent structures (CS) in an unstratified reach of the Snohomish River estuary using in situ velocity measurements and surface infrared (IR) imaging. Sequential IR images are used to estimate surface flow characteristics via a particle-image-velocimetry (PIV) technique, and are conditionally sampled to delineate the surface statistics of bottom-generated CS, or boils. In the water column, we find that turbulent kinetic energy (*TKE*) production exceeds dissipation near the bed but is less than dissipation in the midwater column and that *TKE* flux divergence closes a significant portion of the measured imbalance. The surface boundary leads to divergence in upwelling CS, and leads to the redistribution of vertical *TKE* to the horizontal. Very near the surface, statistical anisotropy is observed at length scales larger than the depth H (3–5 m), while boil-scale motions of O(1)m are nearly isotropic and exhibit a $-5/3$ turbulent cascade to smaller scales. Conditional sampling suggests that TKE dissipation in boils is approximately 2 times greater on average than dissipation in ambient flow. Similarly, surface boils are marked by significantly greater velocity variance, upwelling, divergence, and *TKE* flux divergence than ambient flow regions. Coherent structures and their surface manifestation, therefore, play an important role in the vertical transport of *TKE* and the water column distribution of dissipation, and are an important component of the *TKE* budget.

Citation: Talke, S. A., A. R. Horner-Devine, C. C. Chickadel, and A. T. Jessup (2013), Turbulent kinetic energy and coherent structures in a tidal river, *J. Geophys. Res. Oceans*, *118*, 6965–6981, doi:10.1002/2012JC008103.

1. Introduction

[2] The water surface in rivers is constantly disrupted by boils, which consist of localized upwelling motions that result in super-elevation of the surface and are often adjoined by smaller eddies with vertical vorticity [*Matthes*, 1947; *Coleman*, 1969; *Jackson*, 1976; *Babakaiff and Hickin*, 1996; *Best*, 2005; *Nezu*, 2005]. Their surface morphology can range from flat, weakly spreading "pancake-like" structures to more energetic, "cauliflower-like" and "rams-head" boils [*Babakaiff and Hickin*, 1996]. These boils are the surface expression of bottom-generated turbulent coherent structures (CS); for this reason, boils often contain greater sediment concentrations than the ambient fluid [*Best*, 2005]). Further, boils are important mechanisms for surface water renewal and dispersion [*Nimmo-Smith et al.*, 1999]. As the relative roughness of the bed increases, more intense "boiling" is observed [*Babakaiff and Hickin*, 1996]. However, despite the observed importance of boils to mixing processes, making quantitative surface measurements of boil statistics in the field and linking them to subsurface CS has remained a challenge.

[3] The generation and dynamics of CS has been variously linked to bursting processes in the boundary layer [*Jackson*, 1976; *Yalin*, 1992], packets of hairpin vortices that form in the viscous sublayer of a smooth or rough channel [*Adrian et al.*, 2000; *Hurther et al.*, 2007], and horseshoe-shaped vortices created in the separated flow downstream of dune-crests [*Müller and Gyr*, 1986]. Field measurements attribute the generation of CS to Kelvin-Helmholtz like instabilities in a shear layer generated by flow separation over dune crests [*Kostaschuk and Church*, 1993; *Bennett and Best*, 1995; *Venditti and Bennett*, 2000]. Spanwise, horseshoe-shaped vortices are ejected upward once the separated flow reattaches to the bed [*Nezu and Nakagawa*, 1993; *Kadota and Nezu*, 1999]. Over a large, depth-scale sill, *Chickadel et al.* [2009] and *Talke et al.* [2010] found that boils were linked to flow separation and mixing layer growth.

[4] Near the water surface, CS are affected by the kinematic boundary condition, which stipulates that no flow occurs through the surface. Using a large eddy simulation, *Zhang et al.* [1999] and *Shen et al.* [1999] show that the vertical turbulent intensity approaches zero at the water surface. The vertical velocity variance is redistributed into the horizontal velocity variance, particularly the transverse

---

[1]Department of Civil and Environmental Engineering, Portland State University, Portland, Oregon, USA.
[2]Department of Civil and Environmental Engineering, University of Washington, Seattle, Washington, USA.
[3]Applied Physics Laboratory, University of Washington, Seattle, Washington, USA.

Corresponding author: S. A. Talke, Department of Civil and Environmental Engineering, Portland State University, PO Box 751 CEE, Portland, OR 97207-0751, USA. (s.a.talke@pdx.edu)

component. Laboratory measurements described in *Nezu and Nakagawa* [1993] suggest a 30–40% reduction in the vertical rms velocity $(\overline{w'^2})^{1/2}$ between $z/H = 0.9$ and $z/H \approx 0.98$–0.99, where H is the water depth and z is measured upward from the bed. Numerical estimates from *Shen et al.* [1999] suggest a reduction in w' of $\approx 80\%$ over the same distance. Finally, the semiempirical equation of *Hunt* [1984] suggests that w' is reduced by 54% between $z/H = 0.9$ and $z/H = 0.99$. Hence, the details of the TKE redistribution near the surface are not well characterized, particularly in the field.

[5] The redistribution of turbulent kinetic energy into horizontal components occurs within a "blockage layer" that influences a CS when it approaches to within a radius of the water surface [*Zhang et al.*, 1999; *Shen et al.*, 1999; *Brochini and Peregrine*, 2001; *Troiani et al.*, 2004]. In terms of the turbulent energy budget, laboratory-based studies support a "chainsaw model," in which large-scale eddies serve to transport smaller vortices (turbulent energy) upward, but themselves never reach the surface because of the surface boundary condition [*Moog and Jirka*, 1999]. Instead, the smaller-scale motions, which form the "teeth" of the chainsaw, reach the surface and are important for processes such as air-water gas transfer [see also *Zappa et al.*, 2007]. Additionally, coherent structures are often invoked as an important mechanism for redistribution and transport of TKE within turbulent boundary layers, but few measurements in the field exist that can support this idea. In particular, CS may play an important role in systems where the production and dissipation of TKE do not match locally. *Orton et al.* [2010] found that energy dissipation caused by wind-induced shear dominated over dissipation caused by bottom-generated turbulence at a near surface measurement location (50 cm below surface) in the Hudson River estuary. Near surface turbulence production and dissipation were approximately equal, though a significant upward-directed turbulent transport was noted during less-stratified flood tides. *Scully et al.* [2011] found that estimates of production and dissipation in several East-Coast estuaries were approximately equal in the upper water column, but unequal in the lower water column in areas of high roughness. *Talke et al.* [2010] investigated how the growth of mixing layer (separated flow) and embedded coherent structures are influenced by the surface boundary as water depth over a sill decreases, and conclude that the surface significantly damped growth when the sill height was >80% of the water depth. None of these studies, however, investigate the relationship between CS and the turbulent energy budget.

[6] The objective of the present work is to quantitatively investigate the turbulence characteristics of near-surface CS under unstratified, tidally varying flow conditions. Two terms, coherent structures and boils, are used somewhat interchangeably since they both describe the same geophysical features; however, the term "boils" refers strictly to the surface expression of coherent structures. We use a novel experimental platform that couples infrared remote sensing of the water surface to identify the surface expression of CS with highly resolved colocated near-surface and water column turbulence measurements. This combination enables us to quantitatively link the subsurface turbulent structure with
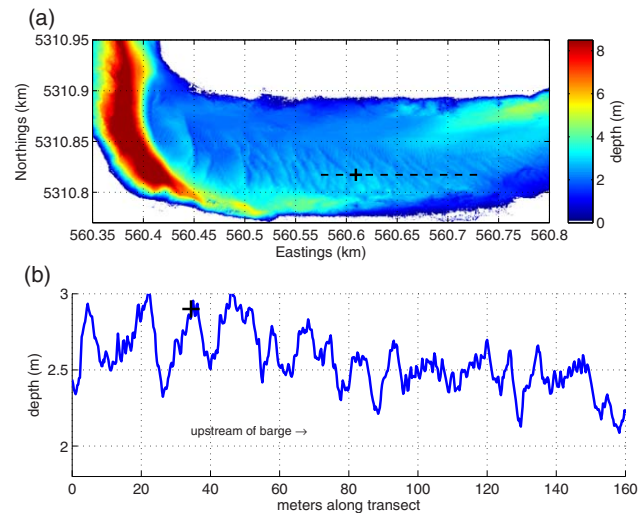

Figure 1. (a) Bathymetry around the experiment site, which is marked with a "+". (b) The bathymetric profile from 560.575 to 560.735 eastings along the dashed line in upper panel; the approximate location of the instrumentation is given by "+". Ebb flow direction is from right to left.

its surface expression and to measure the turbulent kinetic energy (q^2) and its dissipation rate (ε) within boils.

2. Study Site and Background

[7] The Snohomish River Estuary empties into Puget Sound approximately 30 km north of Seattle WA. The tidal range varies between 0.5 and 4 m and is marked by large diurnal and spring-neap variation [*Talke et al.*, 2010; *Giddings et al.*, 2011; *Wang et al.*, 2011]. During the experiment from 8 September 2009 to 25 September 2009, river discharge decreased from 250 to 50 m³/s. We focus here on measurements made during the greater ebb beginning at 9:12 pm local time (4:12 GMT) on 24 September during a period when salinity and stratification effects were negligible.

[8] The measurements were made 16 km from the estuary mouth about 150 m upstream of a large bend (Figure 1), commenced at high water slack and continued for nearly 7 h. Calm and clear atmospheric conditions during the night resulted in a placid, wave-free surface flow broken only by turbulent boils from below; winds of 0.1 ms⁻¹ measured by an anemometer confirm that that wind-wave contamination was negligible. Few vessels were on the water during the nighttime measurement period, minimizing wave and wake disturbances. Hence, both atmospheric and river conditions were ideal for measuring flow and turbulence statistics due only to bottom-generated turbulence. Moreover, the calm and clear atmospheric conditions promoted the growth of a pronounced cool skin layer, which occurs due to outward heat flux from the water surface into the air [*Saunders*, 1967; *Fairall et al.*, 1996].

[9] The primary bathymetric features at the site are semi-periodic dunes with a height d of approximately 0.3 to 0.6 m and wavelengths that varied from 5 to 15 m (Figure 1). Instruments were centered near the crest of a 0.45 m high stoss face on a dune with a trough-to-trough wavelength of
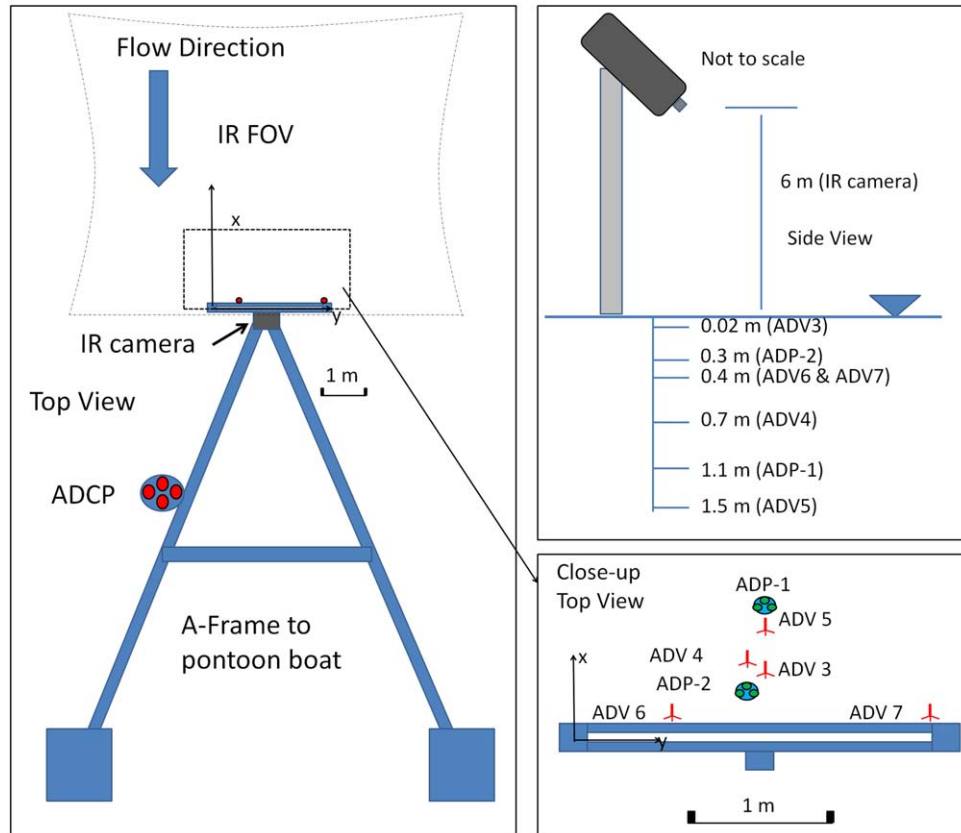
Figure 2. Sampling setup. The frame on the left shows a top view with the A-frame, the IR field of view (FOV), and the location of the IR camera and the ADCP. The close-up top view (bottom right) shows the locations of the five ADVs and two Nortek ADPs used in the experiment. The vertical orientation of the ADVs, the ADPs, and the IR camera are depicted schematically in the upper right frame.

approximately 15 m (instrument location is known only to within 2 m due to GPS accuracy). A large 0.55 m dune crest is located 10 m upstream; however, the dunes approximately 50 m upstream are significantly smaller (0.2–0.4 m), indicating that the flow measurements are in a bathymetric transition zone. Ripples of approximately 1–2 m length and 0.05 m height are overlaid onto the three-dimensional dune field, providing another scale of variability. Since the water depth H decreased from 5 to 2.5 m during the ebb-tide measurement period, the relative roughness d/H from the dunes increased from approximately 0.1 to 0.2. We find that the mean lateral circulation is small compared to the along-channel component, and therefore, surmise that the sharp bend 150 m downstream of the experiment site exerted a negligible influence.

2.1. Measurements

[10] In situ and remote sensing measurements were made from the R/V Henderson, a 65 ft. long research barge. The Henderson floats on two pontoons, which minimizes the flow disturbance caused by the boat, and horizontal motion was eliminated by driving two 2.5 ton spuds into the bed. These spuds allowed the Henderson to float freely up and down with the tide, but minimized boat rocking.

[11] To eliminate any flow disturbance caused by the pontoons, both in situ instrumentation and an infrared remote camera were mounted on the end of a retractable A-frame that extended 6 m upstream of the barge (Figure 2). All instrumentation was cabled and measured in real time, with time synchronized to the GPS signal. The downward looking IR camera obtained images at 20 Hz with a resolution of 512×640 pixels and was attached to a 6 m tower. The resulting image area was 4.5 m by 3.5 m, with a spatial resolution of ~0.75 cm and a temperature resolution of less than 20 mK. At the downstream edge of the field of view, a submersible, T-shaped frame held an array of Acoustic Doppler Velocimeters (ADVs) and velocity profilers, which are described in Table 1 (also Figure 2). Velocity data with correlation values <75% or with unrealistic acceleration values (spikes) were removed. Because wind velocities measured with an anemometer averaged 0.1 m/s, no surface waves were present and the near surface ADVs at 0.02 and 0.4 m below the surface (mbs) produced good quality data with only occasional data outfalls due to instrument surfacing. However, the ADV positioned at 0.7 m mbs produced spiky data with low acoustic correlation values and was not used in the analysis. No vibration modes (frequencies) or waves are observed in velocity spectra, indicating that the frame was rigid and that wind wave and boat wake effects were negligible at the measured frequencies. The exception is one episode of boat wake that occurred at $t = 4$ h. The uncertainty of vertical and horizontal ADV measurements was ± 0.002 ms^{-1} and ± 0.01–0.015 ms^{-1}, respectively, based on the white-noise

Table 1. In Situ Instrument Array Used During Experiment

Instrument	Location of Measured Volume Below Water Surface (m)	Lateral Location Relative to Centerline of A-Frame (m)	Measurement Frequency (Hz)	Notes
Sontek ADV	0.02	0	25	Upward looking
Nortek ADV	0.4	0.65	64	Downward looking
Nortek ADV	0.40	−1.3	64	Downward looking
Nortek ADV	0.70	0	64	Pointed into flow
Nortek ADV	1.50	0	64	Downward looking
Nortek ADP	0.05–1.0 (0.05 m bins)	0	4 or 8	Upward looking, pulse coherent mode
Nortek ADP	0.40	0–1 m (0.05 m bins)	4 or 8	Sideways looking, pulse coherent mode

floor in observed velocity spectra. Instrument positions and orientations were measured with an optical surveying system. Operation in cabled mode allowed ADV measurement parameters such as sampling frequency and measurement range to be adjusted as needed to obtain the best resolution and lowest noise.

[12] In addition to the near surface instrumentation, a downward looking 1200 kHz ADCP (RDI) was attached approximately 3 m downstream of the IR field of view, and run in "Mode 12" with a frequency of 1 Hz and 0.25 m bins. Two additional velocity profilers were attached to the T-frame: an upward looking ADP (Acoustic Doppler Profiler; Nortek) at a depth of 1.05 m, and a sideways looking ADP at a depth of 30 cm (Figure 2). The ADPs sampled in pulse coherent mode at a frequency of 8 or 4 Hz, depending on flow conditions, with 0.05 m bins. Salinity and temperature profiles with depth were made by casting an autonomously measuring SeaBird 19+ Conductivity-Temperature-Depth profiler off the stern in 10–20 min increments throughout every measurement period. The SeaBird 19+ measured at 4 Hz with a temperature accuracy of $\pm 0.005°C$ and conductivity accuracy of ± 0.0005 S/m. Measurements were converted to density using the EOS-80 (Equation of SeaWater, 1980) definition of sea-water.

2.2. IR Analysis

[13] The water surface of a river contains a cool skin layer of <0.001 m thickness [*Saunders*, 1967; *Fairall et al.*, 1996] which is continually disturbed by warmer, subsurface fluid with patterns that are readily revealed by infrared imaging (Figure 3) [*Chickadel et al.*, 2011]. Small-scale convective overturning is observable as centimeter-scale temperature filaments [*Schimpf et al.*, 2004], particularly during slack-water conditions before boils become evident (Figures 3a–3c). Larger warm patches are produced later in the ebb by subsurface turbulent structures that propagate upward and break the water surface (Figure 3 and video in the supporting information) [see also *Chickadel et al.*, 2009, 2011]. As shown by the three consecutive images in Figures 3d–3f, the temperature disturbances change shape and are advected downstream as the boils interact with the surface, thus providing a surface expression of internal boil dynamics. Between and around boils are undisturbed fluid patches, which show darker (cooler) coloration due to preservation of the cool-skin layer. As shown later, the turbulent energy production/dissipation during the slack water period is extremely small, suggesting that the TKE statistics of convective overturning in

Figures 3a–3c are small. Therefore, the effect of convective overturning on the TKE budget during energetic boiling is negligible.

[14] *Chickadel et al.* [2011] used a feature-based PIV algorithm to successfully measure horizontal velocity, horizontal velocity variance, and dissipation at the water surface with errors less than 2%, 8% and 7%, respectively, compared with colocated near-surface (0.02 m depth) velocity measurements. The PIV algorithm used multiple interrogation windows of different pixel size and combined multiple images to produce a 5 Hz velocity signal with an effective resolution of 6 cm × 6 cm (55 × 67 pixels). Occasional errors at the image edges reduce the effective grid size to 3 m (streamwise) by 3.5 m (cross stream). The estimated uncertainty of an individual IR-PIV measurement is $\pm 0.01–0.02$ ms^{-1}, based on the white-noise floor in power spectra taken at each location in the cross-stream (y) direction over each 15 min PIV-IR scene. Measurements with noise floors more than twice the standard deviation of the overall noise-floor were removed. The large number of data points in each 15 min PIV scene—between 2×10^5 and 3×10^5 usable points—explains the good agreement between in situ and surface measurements found in *Chickadel et al.* [2011].

[15] We exploit the IR PIV techniques developed by *Chickadel et al.* [2011] to investigate boil flow and turbulence properties. In situ and surface PIV data are conditionally sampled to distinguish boils from ambient water, defining boils as regions with surface temperature deviations greater than the mean based on the IR images. While simple, we found this technique to be the most robust and unbiased method for independently detecting the occurrence of boils. Other strategies, such as using surface divergence or curl, necessarily use the properties we are trying to characterize. Nonetheless, the binning method has the disadvantage of lumping older boils with newer, more vigorous boils. The boundaries of a boil may also not be clearly delineated, and portions of a boil or free stream that exhibit temperature variance around the mean may be incorrectly attributed. These problems likely mean that the statistical differences between boils and the free stream that we report are under-estimated. To address this issue, we also show selected flow properties as a function of infrared intensity.

[16] We use several techniques to investigate the structure of the surface velocity in the surface PIV data. To visualize the fluctuating velocity field, we remove the spatial average from each IR image. We also estimate the surface
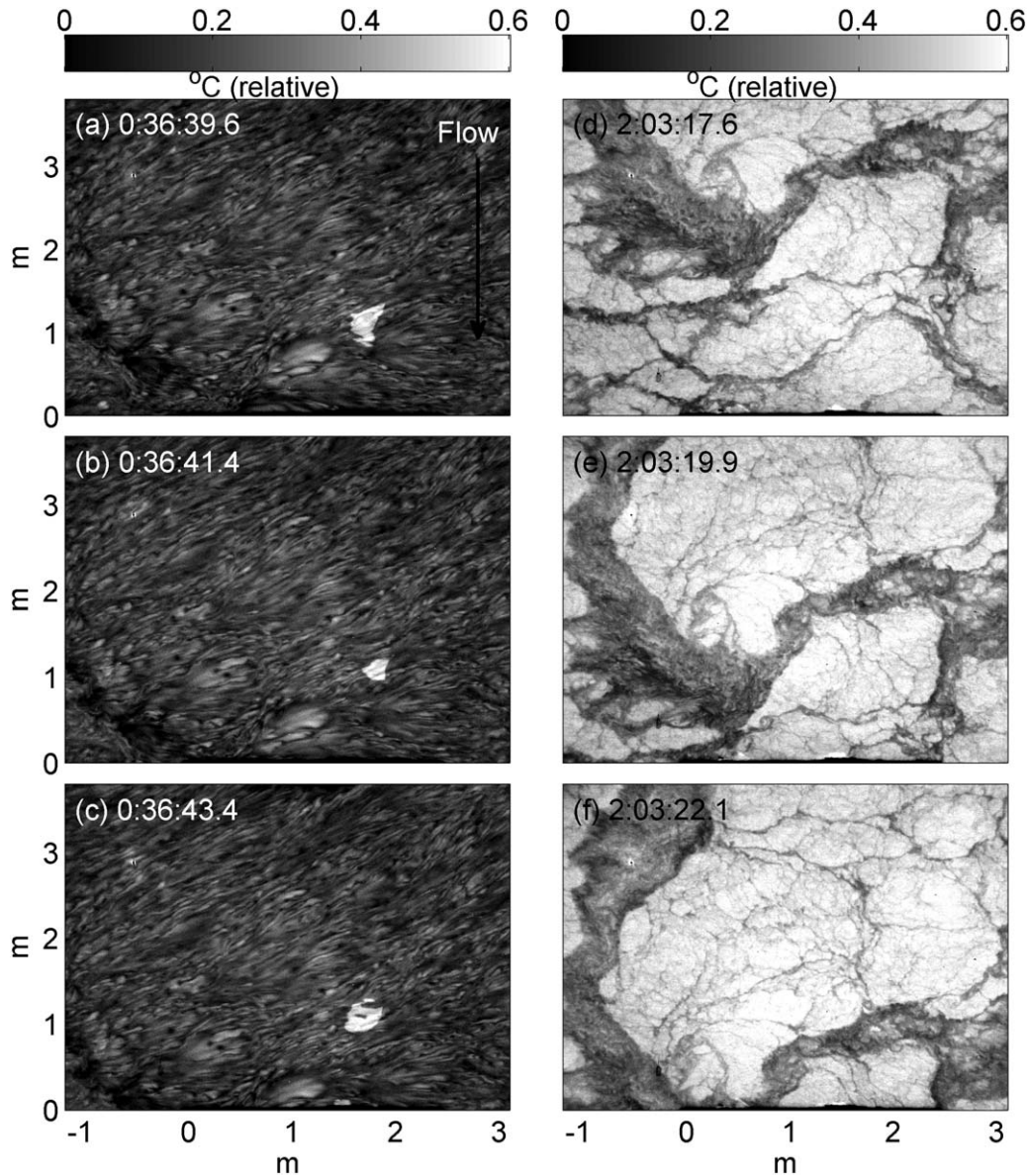
Figure 3. Comparison of surface IR measurements at the beginning of the ebb tide (left) during slack water conditions at 4:48 GMT (flow ~0.1 ms^{-1}) and after 2 h at 6:15 GMT (right). Time $t = 0$ h corresponds to 4:12 GMT. The right side clearly exhibits larger, coherent white areas which occur due to in-situ turbulence (coherent structures) breaking the surface. Early in the ebb, bottom derived turbulence does not reach the surface and the observed thin filaments of elevated temperature are evidence of small-scale convective overturning at the water surface. This convective overturning is also observed between boils (right).

divergence, $dw/dz = -(du/dx + dv/dy)$, and compare this to in situ measurements. The divergence estimate is smoothed by a median filter, reducing the effective resolution to ~0.25 m, and the residual scene-averaged (15 min) divergence is removed to reduce bias. A negative quantity denotes upwelling and divergence, while a positive quantity denotes convergence and downwelling. In all images, x is defined positive in the upstream direction from the lower edge of the IR field of view and $y = 0$ is defined by the center of the I-beam attached to the end of the measurement A-frame. Unless otherwise stated, $z = 0$ is defined at the bed in the figures.

2.3. Turbulent Kinetic Energy

[17] Turbulent kinetic energy (TKE, or q^2) is defined as the sum of the variance of the vertical (w), along stream (u), and cross-stream (v) components of velocity:

$$q^2 = \overline{u'^2} + \overline{v'^2} + \overline{w'^2} \tag{1}$$

[18] Primes denote temporal fluctuations from the mean, which are based on averages over a time period that is large compared to the time scale of turbulent fluctuations. Hereafter, we will use an overbar to denote a time average, and brackets to denote spatial averages. For in situ and surface

IR data we use a 15 min averaging time, which is the time scale of one IR measurement "scene" and is within the standard convention of 10–20 min used for tidal flows [e.g., *Stacey et al.*, 1999]. Near the surface, the vertical rms velocity $(\overline{w'^2})^{1/2}$ becomes increasingly damped [*Hunt*, 1984; *Nezu and Nakagawa*, 1993]. Hence, measurements and theory suggests that *TKE* becomes dominated by horizontal motions near the surface.

[19] Assuming that buoyancy effects are negligible and that horizontal gradient terms are insignificant, the turbulent kinetic energy balance can be written as,

$$\frac{1}{2}\frac{\partial q^2}{\partial t} = T_p + T_d + P - \epsilon, \tag{2}$$

where the rate of change of TKE $= q^2$ is equal to the sum of a pressure transport term (T_p), a diffusive transport term (T_d), the production of *TKE* (P), and the *TKE* dissipation (ϵ). All terms in equation (2) are obtained from our measurements, with the exception of the pressure transport term, $T_p = -\frac{1}{\rho_o}\frac{\partial}{\partial z}\overline{p'w'}$. Scaling suggests that this term could be important at the water surface, since qualitatively estimated surface deflections of order 0.01 m ($p' \sim \rho g \Delta z \sim 100$ Pa) are correlated with measured upwelling velocities w of order 0.05 m/s. The upwelling velocities decay toward zero near the surface, producing a gradient and hence a nonzero T_p (see section 3). Since it is not possible to measure the pressure transport term with our instrumentation, we investigate whether the *TKE* balance can be closed with the remaining terms.

[20] Dissipation ϵ is estimated in the lower and midwater column by applying the structure function method described by *Wiles et al.* [2006] to the along-beam velocities of the ADCP. In this formulation, dissipation is defined by

$$\epsilon = r\left(\frac{D}{C_v^2}\right)^{3/2}, \tag{3}$$

where r is the distance between two velocity measurements, C_v^2 is a constant of order 2.0–2.2, and D is defined by

$$D = \overline{(u'_b(z) - u'_b(z+r))^2}, \tag{4}$$

where u_b is the along-beam velocity (angled at 20° to the vertical) and primes denote a fluctuation from the mean. The set of (r,D) calculated for a particular point z are then used to fit a curve of the form $D(z,r) = N + C_v^2(\epsilon r)^n$, where N is noise and is fit within the range suggested by *Wiles et al.* [2006], and $n = 2/3$ is an exponent. We apply a robust least-squares algorithm that down-weights the effects of outliers and require that the fit is significant to $p < 0.05$. To check that the modeled curve is due to dissipation, we also allow n to be a free parameter and require that its estimated value be between $0.4 < n < 0.9$. The structure function method requires that two points with spacing r have correlated turbulent motions; hence, to minimize the use of uncorrelated motions, we required

that $r < r_{max}$, where r_{max} was the location of the maximum calculated value of D and was approximately equal to κH, where κ is von Kármán's constant. For the dissipation estimates fulfilling the above criteria, the average exponent n was 0.64 with a standard deviation of 0.14, indicating a good fit to data.

[21] In the upper water column, dissipation is estimated from ADV data using the inertial cascade method in which the wave number power spectrum $S(k)$ is related to dissipation ϵ and the wave number k by:

$$S(k) = \alpha \epsilon^{2/3} k^{-5/3}, \tag{5}$$

where $\alpha = 0.67$ for directions perpendicular to the mean flow [*Tennekes and Lumley*, 1972]. We use Taylor's frozen turbulence hypothesis to convert the measured frequency f and power spectrum $P(f)$ at a point to the terms in equation (5) by $k = 2\pi f/\bar{u}$ and $S(k) = \bar{u}P(f)/2\pi$, where $\bar{u}$ is the average advection velocity. A least-squares line with a $-5/3$ slope is then fit to the power spectra to estimate dissipation. Strict application of the inertial cascade method requires isotropic conditions [*Kolmogorov*, 1941]; we show in this manuscript that equation (5) can be applied even close to the water surface. The power spectrum is calculated using a multitaper method [*Percival and Walden*, 1993] over a frequency band of nearly 2 decades. To test data quality, we fit an additional line with an unconstrained slope to the inertial cascade and required that the least-squares slope lie within a range of -1.4 to -1.8. For all ADV data, the average slope for 15 min data segments was -1.61 with a standard deviation of 0.08, indicating good data quality. We also calculated power spectra and estimated dissipation over short time periods of 2–30 s using conditionally sampled data, following the use by *George et al.* [1994] of small sampling windows and a local mean velocity to estimate ϵ in the near-shore environment (see section 3). For these smaller periods the slope-check criteria was relaxed to a slope range of -1.2 to -2.0 to account for spectral noise and a smaller frequency range available for fitting (one decade in frequency space). The average slope for time periods between 2 and 30 s was normally distributed with a slope of -1.62 and a standard deviation of 0.21, indicating a good fit to a $-5/3$ curve.

[22] The production of *TKE* is defined by $P = -\overline{u'w'}\frac{d\bar{u}}{dz}$. We calculate the velocity covariance $-\overline{u'w'}$ from the ADCP using the variance method described in *Stacey et al.* [1999]. For convenience, we hereafter denote the velocity covariance as the Reynolds stress, recognizing that the actual stress is scaled by density. Near-surface estimates of Reynolds stress are computed from the ADV data and production is estimated by combining values with the mean vertical velocity gradient determined using vertically spaced adjacent ADVs.

[23] The vertical *TKE* flux is defined as:

$$F = \frac{1}{2}\overline{w'\Phi}, \tag{6}$$

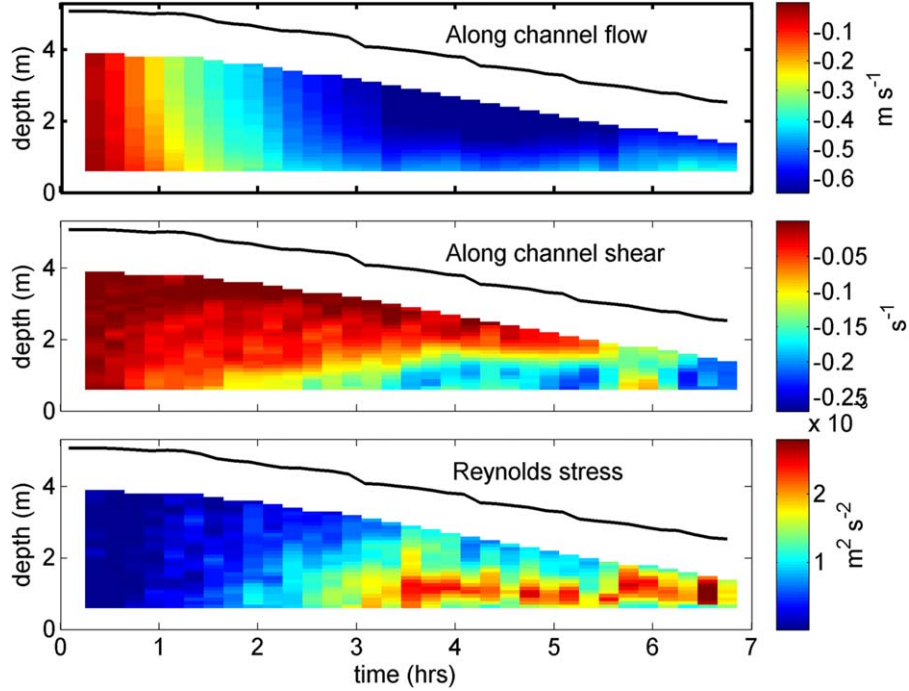where $\Phi = u'^2 + v'^2 + w'^2$, and the vertical *TKE* flux divergence is defined as:

Figure 4. (a) Streamwise velocity, (b) vertical velocity shear dU/dz, and (c) the Reynolds stress on the ebb of 24 September. Time $t = 0$ h corresponds to $4:12$ GMT.

$$T_d = -\frac{\partial F}{\partial z} \qquad (7)$$

[24] Near the surface, the triple correlation in equation (6) is calculated directly from the ADV velocity data and the gradient in equation (7) is computed from vertically spaced ADVs. In the water column, estimates of TKE flux and flux-divergence are generated by applying the method described in *Stacey* [2003] to the ADCP data. This method involves calculating the sum of the third moment of each of the ADCP beams and requires energetic conditions and low noise from disturbances such as waves or boat wakes. Our stable platform and calm night-time conditions allow this method to be applied.

[25] Equation 7 provides an estimate of T_d to within approximately 20 cm of the water surface. However, it is valuable for our understanding of surface flux processes to investigate the role of CS in TKE transport right at the water surface. Although this cannot be measured directly, we next develop an approximation to T_d using only data from the surface IR velocity data. We first assume that vertical velocity fluctuations on the surface are much smaller than horizontal fluctuations, such that $\Phi \approx u'^2 + v'^2$, where u' and v' are defined from the 15 min temporal mean calculated at a particular grid-point of the IR-PIV velocity estimate. Hence, the time average of Φ is the horizontal contribution to TKE. Next, we estimate the vertical velocity gradient dw/dz at the surface for each instance in time using the continuity equation:

$$\frac{dw}{dz} = -\left(\frac{du}{dx} + \frac{dv}{dy}\right). \qquad (8)$$

[26] If divergence is constant over a known depth Δz and surface deflections are negligible, equation (8) can be used to approximate the vertical velocity fluctuations Δw near

the surface. Further, since $\overline{w} \approx 0$ and $w \approx w'$ near the surface, we can approximate the vertical velocity gradient as $\frac{dw}{dz} \approx \frac{dw'}{dz}$. We next define a new quantity T_{IR} by taking the temporal average of the product of Φ and equation (8), after replacing $\frac{dw}{dz}$ by $\frac{dw'}{dz}$:

$$T_{IR} = -\overline{\frac{1}{2}\Phi dw'/dz}. \qquad (9)$$

[27] This quantity, scaled by a factor of 0.5 and with units of (m^2/s^3), represents the correlation between upwelling and the squared velocity anomaly at the surface caused by turbulent motion. Because Φ is positive definite, a positive value of $-\Phi dw/dz$ means that turbulent fluctuations are being brought up to the surface. Similarly, a negative value implies that turbulent fluctuations are being carried down into the water column. Note that the flux of TKE through the material surface is zero. The error in T_{IR} is estimated through a Monte Carlo technique whereby a 15 min IR-PIV scene is resampled by perturbing each measured (u,v) by a randomly sampled value from a normal distribution with a standard deviation of 0.01–0.02 ms^{-1} (the measurement uncertainty). T_{IR} estimates made from a total of 1000 ensembles show that the standard deviation averaged 6%, with a range from 3 to 11% and one outlier of 20% during the early ebb (section 3).

[28] If we assume that $\Phi(z)$ is nearly constant at the surface, or equivalently that the turbulent flux divergence at the surface is dominated by the gradient in turbulent vertical velocity w', we can approximate the divergence of turbulent flux in equation (7) as:

$$T_d \approx -\frac{1}{2}\left(\overline{\Phi \frac{d}{dz}w'}\right) = T_{IR} \qquad (10)$$

[29] Note that $\Phi(z) \approx$ constant was shown in *Chickadel et al.* [2011] by the good agreement between the near
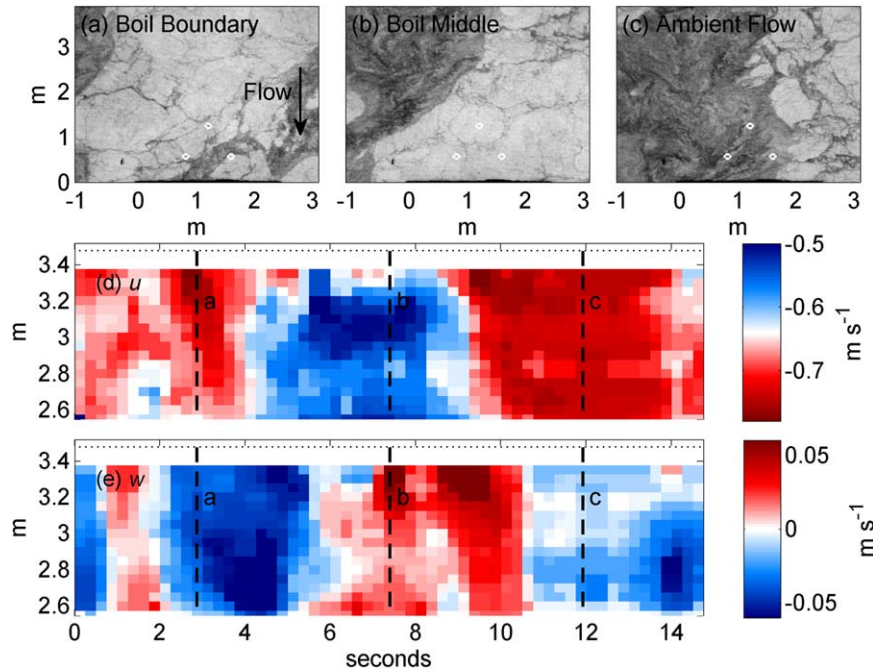
Figure 5. Snapshots of a boil (a, b, c) advecting down through the field of view (current direction is in the minus y axis direction) at approximately 8:42 GMT ($t = 4.5$ h). The corresponding horizontal and vertical velocity from the Aquadopp profiler (ADP) are shown in Figures 5d and 5e. The water surface in Figures 5d and 5e is shown by a dotted line. The footprint of the three beams of the ADP are shown by white circles in Figures 5a–5c. Depth is measured upward from the bed. The temperature scale of Figures 5a–5c is given in Figure 3.

surface ADV (0.02 mbs) and the surface IR measurements. We therefore hypothesize that T_{IR} (equation (9)) is a reasonable approximation for TKE flux divergence T_d at the surface, and can be used in combination with conditional sampling to separate the effects of boils and ambient water on the TKE balance at the water surface. We check this hypothesis and the assumptions outlined above later in the manuscript.

3. Results

3.1. Coherent Structures In Situ and at the Surface

[30] During the greater ebb tide on 24 September, flow increased from zero at high water slack to a depth-averaged maximum of 0.6 m/s at $t = 4$ h, then decreased to approximately 0.5 m/s over the subsequent 3 h (Figure 4). Depth decreased from 5 to 2.5 m over the 7 h measurement period (Figure 4a). The largest shear occurs in the bottom portion of the water column and becomes more intense even after the maximum surface velocity period (Figure 4b). Reynolds stress is highest near the bed, and decreases approximately linearly upward (Figure 4c). The mean lateral component of flow was <2–3% of the along-channel flow for all but the first and last 20 min of the measurement period. Occasional boils were observed beginning approximately 0.5 h after high water slack, when the velocity and depth were 0.1 m/s and 5 m, respectively; beginning about 1 h after high water slack, boils were consistently observed on the water surface (see Figure 3).

[31] A pattern of upwelling flow alternating with downwelling flow is observed in both surface IR measurements of boils and near surface ADP measurements (Figures 5 and 6). Because the ADP velocity measurement is an average of 3 beams, only large-scale motions (>0.5–1 m) are coherent in Figure 5. As a large, warm patch of boils begins to advect over the ADP (Figure 5a), flow in the upper 1 m of the water column (Figures 5d and 5e) is both fast (−0.7 to −0.75 m/s) and directed downward (−0.04 m/s). In the middle of the patch (Figure 5b), flow is much slower (−0.5 to −0.6 m/s) and is directed upward (0.04 m/s). After the patch passes (Figure 5c), near-surface flow returns to the free stream velocity (−0.7 m/s), the water temperature becomes cool, and the vertical velocity tends toward zero. The size of the slow patch observed in the ADP (Figure 5d) is similar to the observed size of the surface patch of boils (Figures 5a–5c), and both are slightly smaller than the water depth of 3.5 m. Within the water column, a statistical cross-correlation analysis of the along-beam ADCP velocity, which extends through much of the water column at 20° from the vertical, suggests that statistically significant correlation is measured out to a 1.5 m lag for the period in Figure 5. This observed scale is similar to Prandtl boundary layer scaling ($\kappa H \sim 1.5$ m, where $\kappa =$ von Kármán's constant and $H = 3.5$ m), and is closer to the typical boil size observed in Figures 3 and 6 but about half the size of the patch of boils in Figure 5. The integral length scale in the along-beam ADCP data was 0.8 m for the period in Figure 5, and ranged from 1 m ($t = 2$ h) to
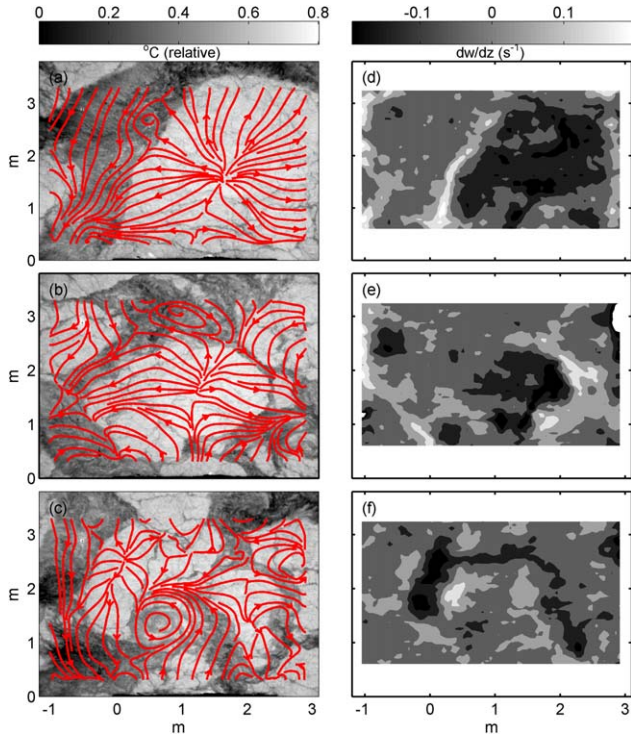
Figure 6. (a–c) Examples of three infrared images and (d–f) associated divergence dw/dz between 6:14 and 6:18 GMT ($t = 2$ h). Streamlines with the spatial mean removed are overlaid on the IR images. The streamlines show areas of negative divergence (upwelling), positive divergence (downwelling). Flow direction is from top to bottom (negative direction).

0.65 m ($t = 6$ h) (Figure S5). Therefore, the dimension of a typical CS in the water column appears to be smaller than its surface expression. This may occur because packets of CS, which occur in the water column [see *Adrian et al.*, 2000], tend to amalgamate at the surface to make a larger patch of boils (see Figures 3, 5, and 6, and video in supporting information).

[32] The pattern of upwelling and downwelling associated with boils is also observed in surface velocity streamlines (Figure 6). Using the PIV-IR flow estimates, we define local fluctuations $\tilde{u}$ and $\tilde{v}$ by removing a spatial average of the velocity in each PIV-IR field. Streamlines of the mean-removed flow are overlaid on IR temperature maps. Boils are marked by divergent streamlines emanating from a common source, while ambient flow is characterized by either parallel streamlines or rotational flow (Figures 6a–6c). Positive is defined in the upstream direction (see section 2.2.).

[33] The divergence dw/dz shown in Figures 6d–6f shows that the center of a boil is marked by upwelling flow (negative dw/dz). At the boundary of boils and ambient fluid, thin convergent zones (positive dw/dz) are observed (much as in Figure 5), likely due to the collision of outward expanding flow in the boil-patches and cooler, ambient water, with a different flow structure. Eddying motion (vorticity) is also observed in Figure 6 in the ambient (nonboil) region, probably due to shear between boils and the ambient flow [*Best*, 2005]. The correspondence between the ADCP beam fluctu-

ations, the ADP velocity structure, and the IR temperature/flow measurements suggests that CS signatures are found throughout the water column and at the surface.

3.2. Statistical Properties of Surface Coherent Structures

[34] The observations in Figures 3, 5, and 6 suggest that the boils are surface manifestations of turbulence and coherent structures from lower in the water column, from which they inherit both their temperature and flow statistics. In Figure 7, we show the surface distribution of along-stream velocity (u), divergence (dw/dz), and the squared velocity anomaly Φ (equation (6)) as a function of the temperature anomaly. A positive temperature denotes a boil, while a negative temperature denotes an ambient flow region.

[35] Results show that the average velocity of a boil is approximately 4% or 0.02 m/s slower than the ambient flow (Figure 7a). A significant percentage of the warm water boils have flow velocities that are >10% slower than the mean flow, and overall the variance in boils is larger. Within boils, flow velocities are skewed toward slower magnitudes and have a positive skewness of 1.7 (Figure 7a). These active boils thus bring low momentum fluid from deeper in the water column to the surface.

[36] On average, warm patches (boils) also exhibit net upwelling and negative divergence (average -0.02 s^{-1} at $-0.15°$C in Figure 7b), while ambient flow exhibits net downwelling and positive divergence (average 0.02 s^{-1} at $0.2°$C in Figure 7b). Divergence observed in boils exhibits large variability (standard deviation of $0.08–0.1$ s^{-1}) relative to ambient flow (standard deviation $0.04–0.05$ s^{-1}) (Figure 7b). These results are consistent with the qualitative observation that upwelling warm-water patches are
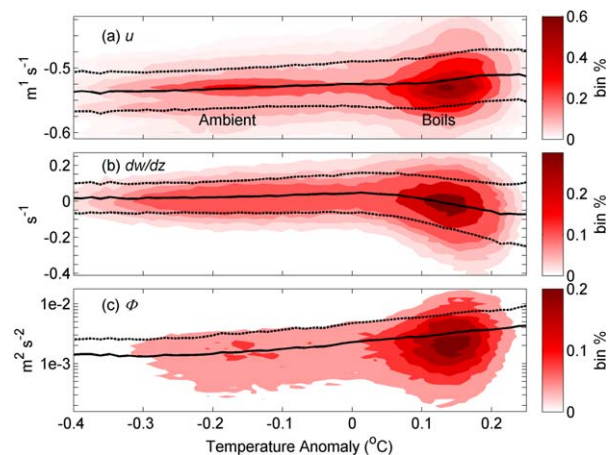

Figure 7. Three dimensional histogram of along (a) channel flow velocity, (b) divergence dw/dz and (c) flow variability Φ versus IR surface temperature. The color scale indicates the percent of the time a value was measured within a bin defined by temperature and a y axis value (i.e., u, TKE, or dw/dz). The standard deviation around the mean is shown by dotted lines. Results are from 6:15 to 6:30 GMT, 2 h after high water. The temperature anomaly is the deviation from the mean-removed surface temperature signal; boils are indicated by a positive anomaly.
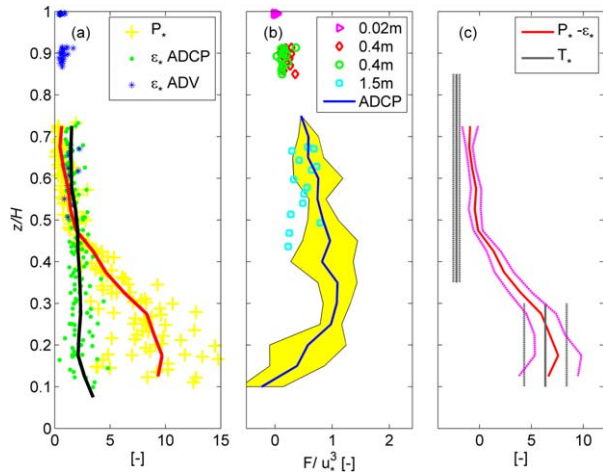
Figure 8. (a) The normalized distribution of dissipation $\varepsilon_* = \varepsilon H/u_*^3$ and $P_* = PH/u_*$,(b) the TKE flux F, and (c) comparison of the TKE flux divergence $T_* = -T_d H/u_*^3$ and the difference between normalized production and dissipation. Results are evaluated between $t = 2$ h and $t = 5.5$ h. Turbulent flux measured by the ADCP and the ADVs at 1.5 and 0.4 m below the surface. The standard deviation of F is indicated by yellow fill (Figure 8b), and 95% confidence intervals are shown by dotted lines in Figure 8c. The confidence interval for T_* was calculated by bootstrapping the slope estimate of turbulent flux.

surrounded by downwelling/convergence at its boundary and in ambient fluid (see Figures 5 and 6).

[37] The greater variability of divergence in boils is correlated with greater turbulent velocity variability. Indeed, active boils with a temperature anomaly >0.1°C contain the largest squared velocity anomaly Φ (Figure 7c). Similarly, the smallest Φ values are associated with the coolest temperature anomaly (Figure 7c). At the most probable boil temperature (+0.15°C), TKE is estimated to be 3.0×10^{-3} m²/s²; by contrast, an average TKE of 1.5×10^{-3} m²/s² is found at −0.2°C, the most probable ambient condition. An f test and t test shows that the results are statistically different, and we conclude that the TKE in warm water (boils) is approximately twice the TKE in the ambient (cool water) flow surrounding them. The average TKE for this time period was 2.4×10^{-3} m²/s² and was slightly skewed toward the boil value.

3.3. Turbulence Properties

[38] The water-column TKE budget is investigated in Figure 8, which shows non-dimensional production $P_* = P/(u_*^3/H)$, nondimensional dissipation $\varepsilon_* = \varepsilon/(u_*^3/H)$, nondimensional TKE flux $F^* = F/u_*^3$, and nondimensional TKE flux divergence $T_* = -T_d/(u_*^3/H)$ as a function of z/H during the energetic period between $t = 2$ h and $t = 5.5$ h. The friction velocity u_* is defined by extrapolating a least squares fit to the Reynolds stress to the bed, i.e., $u_* = \sqrt{\left(-\overline{u'w'}\right)_{bed}}$. The results show that an imbalance occurs between profiles of P and ε, with P larger near the bed and ε larger in the midwater column (Figure 8a). The variation stems from a differing functional dependence in the water column: while ε decreases approximately linearly

with height above the bottom, P decreases approximately as $1/z$.

[39] The local imbalance between P and ε implies that other terms in the TKE equation must be significant. While the time rate of change of TKE (left hand side of equation (2)) is $\sim 10^{-7}$ m² s^{-3} and is much smaller than P and ε, estimates of TKE flux (equation (6)) have a substantial nonzero gradient (Figure 8b). Below $z/H = 0.3$, TKE is exported (positive slope), whereas higher in the water column TKE is imported (negative slope). The good agreement between ADV and ADCP estimates in Figure 8 suggests that the TKE flux estimates are reasonably robust.

[40] The normalized turbulent flux divergence T_* is next estimated based on the slope of a linear least-squares fit to TKE flux below $z/H = 0.3$ and another above $z/H = 0.3$ (the scatter in the data precludes higher-order polynomial fits). The data is resampled with bootstrapping to obtain 95% confidence intervals to the estimated slope. Below $z/H = 0.3$ m, $T_* = 6.4 \pm 1$, representing export of TKE from the near-bed region. Above $z/H = 0.3$, $T_* = -2.2 \pm 0.15$, representing an import of TKE from below. For comparison, the quantity $P_* - \varepsilon_*$ is approximately 6.7 ± 0.8 and -0.6 ± 0.25 below $z/H = 0.3$ and above $z/H = 0.45$, respectively. Therefore, our estimated TKE flux divergence closes the measured imbalance in P and ε below $z/H = 0.3$ and provides a mechanism to move excess TKE produced near the bottom upward, where it is subsequently dissipated. In the midwater column, the P- ε deficit is less than TKE flux divergence, which may indicate that other TKE components, such as the pressure term, become important. However, it may alternately reflect the smaller signal-to-noise ratio away from the bed.

[41] Integrated over the water column, T_d is nearly zero to within the confidence interval, which suggests that $P = \varepsilon$ to first order in a depth-integrated sense. On the other hand, the depth-integrated $P - \varepsilon$ deficit is positive, indicating that more TKE is produced than is dissipated. While this suggests that the water column was not in equilibrium and that other terms in the depth-integrated balance are important, *Wiles et al.* [2006] noted that the structure function method used here systematically under-predicted the dissipation ε obtained by other methods.

[42] The IR-based observations in Figure 7 suggests that surface boils are upwelling (transporting) elevated TKE from lower in the water column, consistent with observations of TKE flux and flux divergence in the water column (Figure 8). ADV measurements of $\overline{u'^2}$, $\overline{v'^2}$, and ε over a tidal period show that the average turbulence statistics are approximately 2-3 times less near the surface (0.02 m below surface) than at 1.5 mbs (Figure 9). Similarly, average horizontal variance components were 40–60% larger at 0.4 mbs than 0.02 mbs. A representative parcel of fluid transported unaltered upward from 0.4 or 1.5 mbs (approximately midwater column) to the surface by a CS might, therefore, have TKE that is approximately O(50)% or O(200)% larger, respectively, than the average surface TKE. This order of magnitude is similar to the observed difference between boils and ambient turbulence properties (Figure 7), and we infer that boil properties are sourced from at least the midwater column (see also Figure 5).

[43] Our measurements of vertical velocity variance $\overline{w'^2}$ near the surface show that it is attenuated by 40% ± 8%
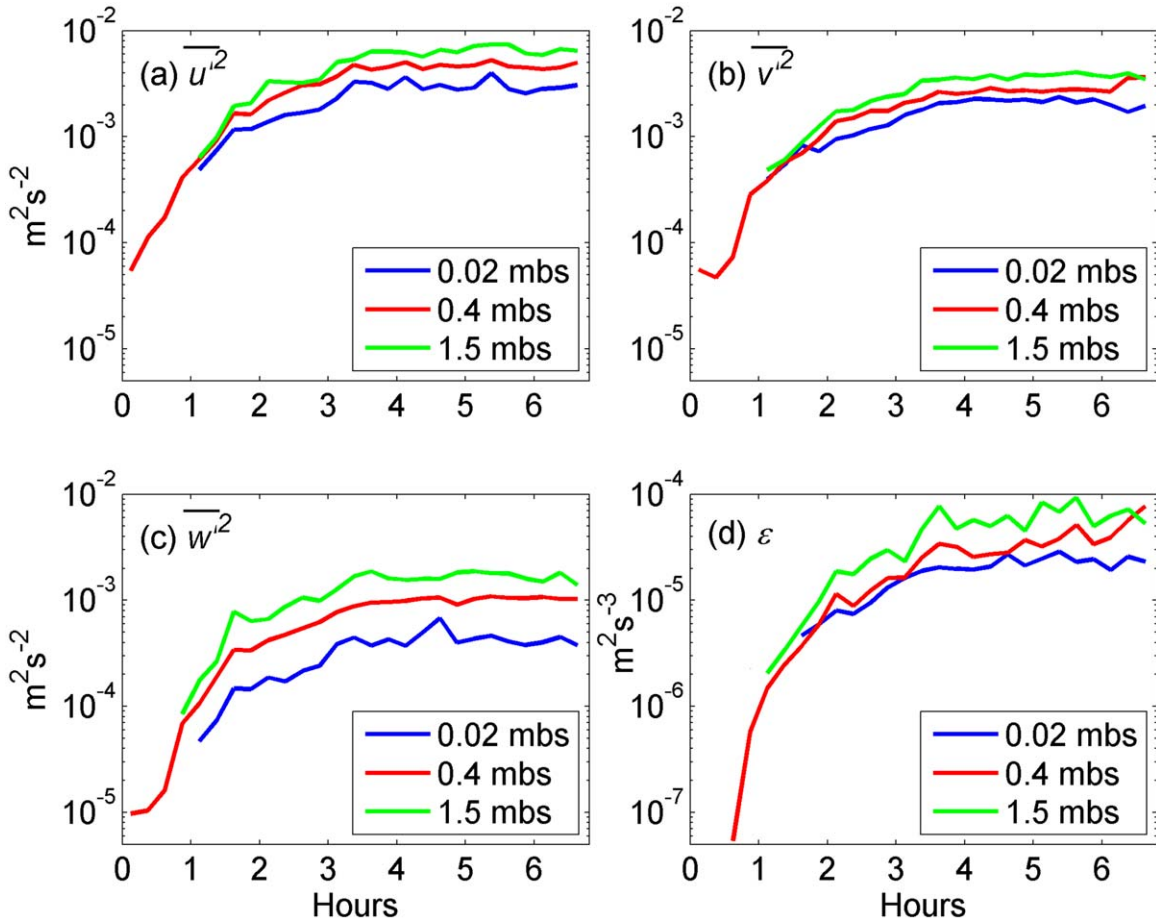
Figure 9. Tidal variation in $\overline{u'^2}$, $\overline{v'^2}$, $\overline{w'^2}$, and ε during the ebb tide period measured 0.02, 0.4, and 1.5 m-below-surface (mbs).

between 1.5 and 0.4 mbs, but $60\% \pm 7\%$ between 0.4 and 0.02 mbs (an average 75% reduction between 1.5 and 0.02 mbs). The differential decrease in $\overline{u'^2}$ and $\overline{w'^2}$ in the upper water column is a clear indication of the kinematic boundary condition. Note that ε is reduced by 60% in the upper 1.5 m of the water column (Figure 9). The causes and implications of a nonzero vertical variance near the surface are discussed further in section 3.5.

3.4. Conditional Sampling of Boils for Dissipation

[44] To investigate the influence of water-column CS on the observed *TKE* statistics, we use the IR signal to segregate surface flow into boils (positive IR temperature anomaly, IR') and ambient fluid (negative IR temperature anomaly). These time periods are then used to conditionally sample the data acquired with the ADV located at 0.02 mbs. The ADV allows investigation of near surface, high frequency fluctuations because of its small sample volume (<1 cm^3), large sampling rate (25 Hz), and low noise floor in the vertical (0.002 ms^{-1}). Examples of four power spectra of vertical velocity during different tidal phases are shown in Figure 10 for both boils (IR$' > 0$) and ambient flow (IR$' < 0$), along with their 95% confidence interval. Elevated vertical velocity variance is observed in boils relative to the ambient flow at all frequencies, consistent with the observations in Figure 7. The high frequency slope in

both ambient and boil spectra is close to $-5/3$ (Figure 10), suggesting that a turbulent cascade is resolved in these short time sequences. Using the inertial subrange method, we estimate that ε is two to three times larger in the boil examples shown in Figure 10 than in the ambient free stream.

[45] The observation that boils, and by extension CS, exhibit larger rates of TKE dissipation is further confirmed by estimating ε in many examples of boils and ambient fluid over the entire measurement period (Figure 11), using the method described for Figure 10. To obtain sufficient data to resolve the inertial cascade and estimate ε, but retain enough boil instances to obtain statistics for each time period, we evaluated continuous windows of positive or negative IR anomaly that were at least 2 s long (roughly corresponding to patches >1 m). Approximately, 30–60 time periods were evaluated for each of the points in Figure 11.

[46] Over the entire ebb tide, the average ε in boils is two to three times larger in a boil than in the ambient fluid (Figure 11b). Similarly, $\overline{w'^2}$ is up to three times larger in boils than the ambient. This observation highlights the role that boils have on the near surface TKE budget and in transporting TKE from regions of larger TKE, which occur lower in the water column, to regions of smaller ambient TKE. The statistically significant difference between ε in boils and the ambient fluid suggests that surface dissipation is patchy on
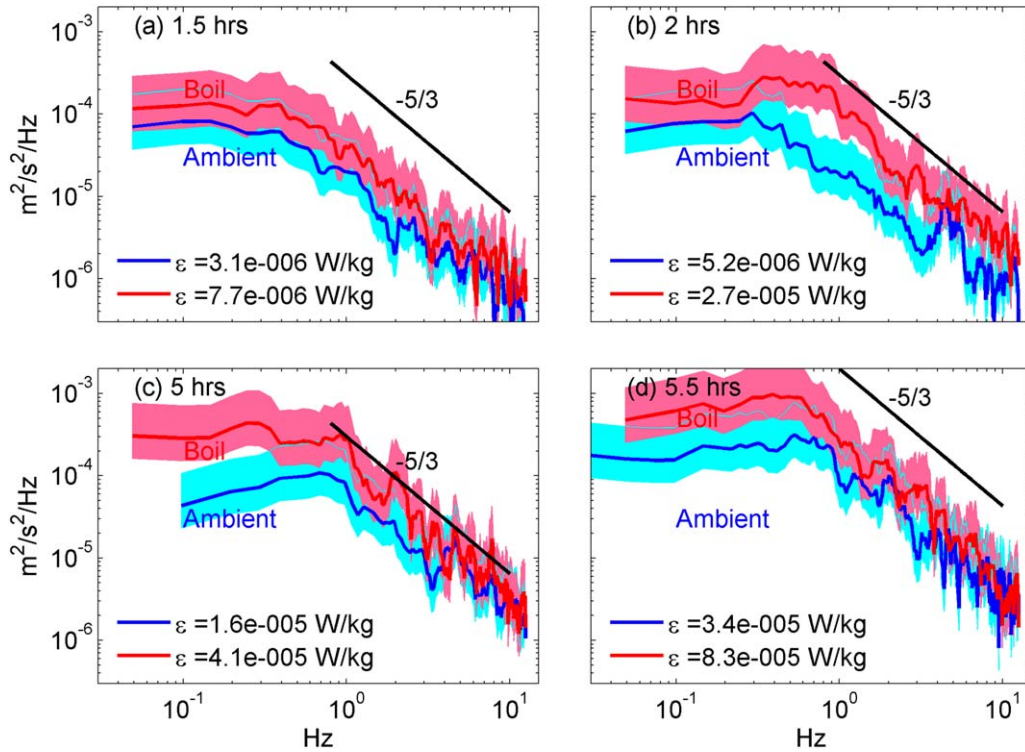
Figure 10. Examples of velocity spectra from the ADV at 2 cm below the surface. The IR data was used to conditionally sample boils (in red) and ambient flow (in blue). Shaded regions denote the 95% confidence interval in the spectral density.
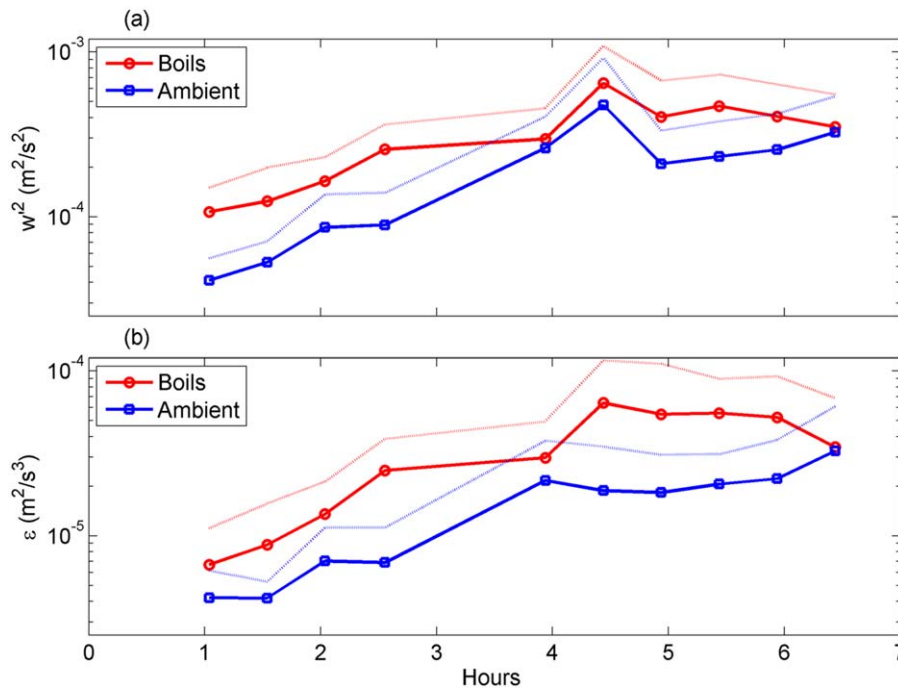

Figure 11. (a) Vertical variance and (b) turbulent kinetic energy dissipation rate binned by boil periods (detrended IR > 0) and nonboil periods (detrended IR < 0). Time is from HW slack. The standard deviation is shown by the dotted line. Estimates are from an ADV with a measurement volume at 0.02 mbs and measuring at 25 Hz.
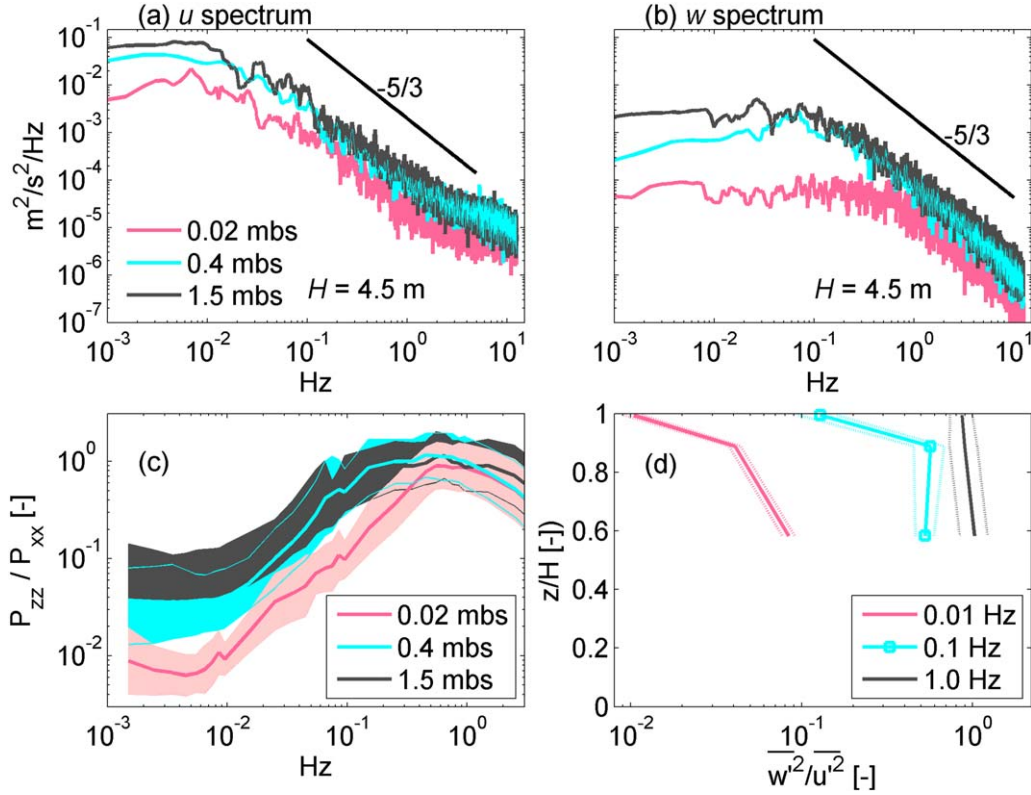
Figure 12. (a and b) Spectra of horizontal and vertical velocity and (c) their ratio averaged between $t = 2$ h and $t = 6$ h. The filled bands in Figure 12c denote the standard deviation of all spectra, which are based on 15 min time intervals. The vertical anisotropy profile as a function of z/H and frequency is shown in Figure 12d, with dotted lines denoting the standard deviation.

the water surface with a length scale on the order of the boil length scale. Hence, adjacent patches of surface water can have significantly different vertical variability and dissipation.

3.5. Anisotropy

[47] The anisotropy ratio, defined as the ratio of vertical to horizontal velocity variance, $\left(\overline{w'^2}/\overline{u'^2}\right)$ provides an indication of the degree to which the surface boundary redistributes vertical motions into horizontal. Purely 2-D horizontal turbulence would have a ratio of $\left(\overline{w'^2}/\overline{u'^2}\right)=0$, while isotropic turbulence would have a ratio of $\left(\overline{w'^2}/\overline{u'^2}\right)=1$. Using the ADV data, we find that $\left(\overline{w'^2}/\overline{u'^2}\right)$ varies from 0.1 to 0.15 at 0.02 mbs to a maximum of 0.25 to 0.35 in the mid water column. Hence, the vertical component of *TKE* is redistributed into horizontal components as the surface is approached (see Figure 8 and supporting information). The observed midwater column values are consistent with the ratio $\left(\overline{w'^2}/\overline{u'^2}\right)=0.3$ that *Nezu and Nakagawa* [1993] report for much of the outer layer flow in open channel flow. For the 3 ADVs located at 0.4 and 1.5 mbs, the mean ratio of cross-channel to along-channel variance $\left(\overline{v'^2}/\overline{u'^2}\right)=0.5-0.55$ over the tidal period (see Figure 9). This agrees well with the *Nezu and Nakagawa* [1993] value of $\left(\overline{v'^2}/\overline{u'^2}\right)=0.5$. At 0.02 mbs, our measured $\left(\overline{v'^2}/\overline{u'^2}\right)$ increases to ~0.68, with a standard deviation

0.07. This increase occurs because boils symmetrically expand outward from their upwelling point. Hence, cross-channel fluctuations receive relatively more energy than along-channel fluctuations, compared to the deeper regions below the blockage layer.

[48] An interesting observation from Figures 9 and 11 is that a finite vertical velocity variance (10–15% of the along-channel variance) exists at 0.02 mbs, despite the kinematic boundary condition that enforces no vertical flow at the material surface. The elevated $\overline{w'^2}$ observed in boils (Figure 11) suggests that upwelling CS drive this measurement, perhaps through the formation of small waves at the boil edge due to "erupting turbulence" and surface deflections due to turbulent pressure variations (see e.g., review by *Brochini and Peregrine* [2001] and *Nezu and Nakagawa* [1993]). The observation of nonzero, near-surface $\overline{w'^2}$ has also been found in laboratory open channel flow [*Nezu and Nakagawa*, 1993] and energetic surfacing jets [*Larocque et al.*, 2009], where observations suggest that vertical variance is >25% and >50% of the midwater column value, respectively, at $z/H = 0.98-0.99$. Our measurements confirm this order of magnitude, though further research is needed to determine the reasons for the variability between studies. One possibility, as *Brochini and Peregrine* [2001] note, is that gravity and surface tension constraints become less effective at producing a blockage layer as turbulence becomes more energetic, causing the surface boundary conditions to be enforced in a thin
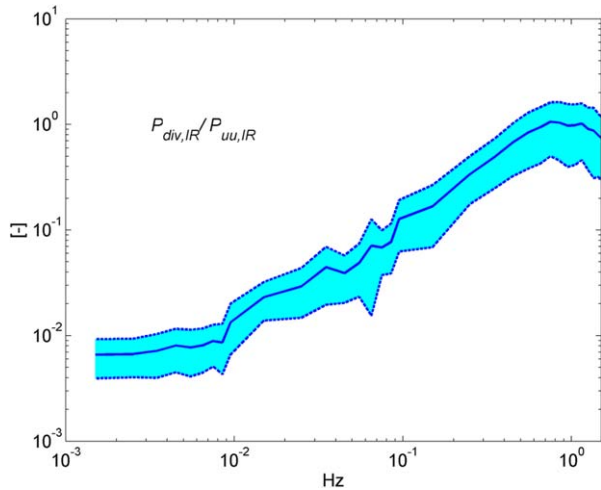
Figure 13. Ratio of the the IR-PIV divergence spectrum ($P_{div,IR}$) and along-channel IR-PIV velocity ($P_{uu,IR}$). The divergence dw/dz has been prescaled by an arbitrary length scale $h_{div} = 0.15$ m, such that the maximum spectral density is unity and the ratio is dimensionless. The shaded area denotes the standard deviation of 50 cross-sectional locations from which 15 min spectral data were obtained.

viscous boundary layer that has a negligible size relative to surface distortions.

[49] Comparing vertical (P_{ww}) and horizontal velocity (P_{uu}) power spectra (Figures 12a and 12b), we find that the change in anisotropy near the surface is produced by a reduction in low frequency vertical fluctuations. This is observed in the marked roll-off, or flattening, of the intensity of P_{ww} at 0.02 mbs at low frequencies <1 Hz (Figure 12b), which indicates that low frequency contribution to vertical velocity variance is small or negligible. These qualitative observations are quantified in Figure 12c, which shows that the average ratio of vertical and horizontal spectra (P_{ww}/P_{uu}) at 0.01 Hz between $t = 2$ h and $t = 6$ h is approximately an order of magnitude smaller at 0.02 mbs than at 1.5 mbs. By contrast, vertical and horizontal spectra at these two depths are approximately equal at 1 Hz. The spectra at 0.4 mbs trace a line between the midwater column (1.5 mbs) and near surface (0.02 mbs) extremes. Hence, low frequency motions are increasingly filtered out in a blockage layer as the surface is approached. This result is confirmed in Figure 12d, which shows that the P_{ww}/P_{uu} ratio varies only slightly with depth at 1 Hz, but is greatly diminished between the midwater column and the near surface at 0.01 Hz. Motions with a frequency of 0.1 Hz are only damped in the upper 10–15% of the water column (i.e., above 0.4 mbs). Results for greater than 2 Hz are not shown because the larger horizontal noise floor begins to bias the P_{ww}/P_{uu} ratio. This is observable as an inflection in the P_{uu} spectral slope around 2 Hz, as the spectrum approaches the noise floor of $\sim 10^{-5}$ m^2 s^{-2} Hz^{-1}. For frequencies of 1 Hz and below, the signal to white noise ratio is >10 and we infer no significant bias in the P_{ww}/P_{uu} ratio due to noise. Because the bulk anisotropy in the water column is similar to canonical estimates [e.g., *Nezu-Nakagawa*, 1993] we infer that there is no systematic bias in

Figure 12, although smaller scale variation due to differences in spectral slope behavior may occur.

[50] Using the Taylor frozen turbulence hypothesis ($U \approx 0.5$ ms^{-1}) to convert frequencies into a length scale, we find that the near-surface variance ratios in Figure 12 correspond well to length scales also observed in surface IR measurements and subsurface ADCP measurements. Whereas no boils are observed at the river width scale of 50–100 m scale (≈ 0.01 Hz in frequency space), boils with a length scale of 1 m (≈ 0.5 Hz in frequency space) are ubiquitous features of the water surface (see Figures 3, 6, and 7). Hence, we surmise that the near unity of P_{ww}/P_{uu} between 0.5 and 2 Hz in Figure 13c is associated with the upwelling action of CS and the corresponding downwelling required by continuity, which occurs at the 1–3 m scale both vertically and horizontally (Figures 5, 6, and 7). The intermediate scale of 5 m (0.1 Hz) corresponds to the largest conglomeration of boils at the surface (e.g., Figures 3 and 5) and still produces some vertical variance near the surface (Figure 12d).

[51] Since the integral under the curves in Figure 12c is the bulk anisotropy ratio ($\overline{w'^2}/\overline{u'^2}$), the results in Figures 12c and 12d can be interpreted as showing anisotropy as a function of frequency. In this interpretation, motions that advect past the ADVs with a 1 Hz frequency (i.e., boils) produce an approximately isotropic signal even 0.02 mbs from the surface. Figure 5 suggests that the vertical extent of subsurface CS are of a similar length scale as the horizontal scale in boils, as required for isotropy. Further, the surprisingly high level of near-surface isotropy at the O(1 m) scale is possible because of boil-scale motions that deflect the free surface.

[52] If correct, this interpretation also implies a relationship between the horizontal velocity variance and the divergence at the surface, since the latter is related to surface deformation. To corroborate the ADV-based result in Figure 12, we next examine the ratio of a power spectra derived from surface divergence dw/dz to the power spectra of along channel velocity (u) for IR-PIV data taken at $t = 5$ h. To obtain a nondimensional ratio, divergence dw/dz was premultiplied by a length scale $h_{div} = 0.15$ m, which was chosen such that the maximum spectral ratio from an average of 50 cross-sectional locations is unity. This length scale is about 5% of the water column depth and can be interpreted as a characteristic length scale over which $w \approx w'$ is damped. This scale is qualitatively consistent with the reduction of anisotropy in the upper 8–10% of the water column observed in the ADVs (see Figure 9; Figure S2 in supporting information).

[53] Results show that the IR-PIV spectral ratio (Figure 13) correlates nearly exactly with the ADV spectral ratio estimated at 0.02 mbs (Figure 12c): low frequencies such as 0.01 Hz have a ratio that is 2 orders of magnitude smaller than at 1 Hz, indicating that upwelling is occurring at O(1 m) scales but not at river-width scales. Figure 13, therefore, substantiates the frequency dependence of the 0.02 mbs spectral ratio (Figure 12c) and leads credence to the ADV results and hence the interpretation that the vertical velocity variance in boils is nearly equal to the horizontal velocity variance (Figure 12d). As before, we note that some small bias may enter the horizontal spectra due to a larger noise floor.
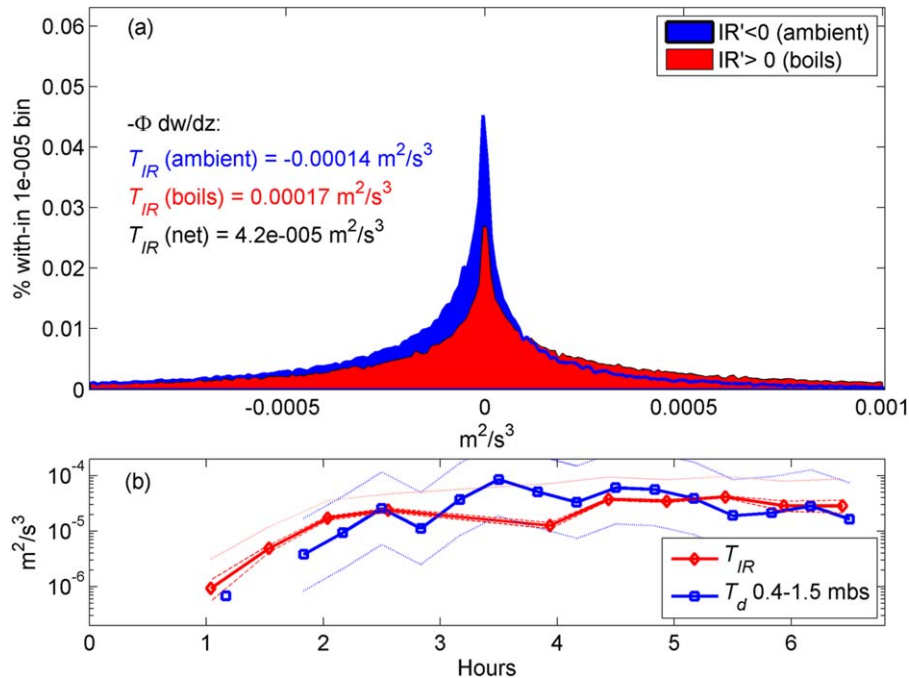
Figure 14. (a) Comparison of the quantity $-\phi\frac{dw}{dz}$ obtained in both boils and ambient flow and (b) a comparison of turbulent transport obtained from in situ ADVs and the transport estimate T_{IR}. The time period is $t = 5.5$ h after HW. The dashed line around TIR (red) and the blue dotted line around T_d represent error estimates.

[54] While the bulk of evidence presented here using different types of measurements (in situ and surface) supports the interpretation of near-surface isotropy for boil scales and smaller, it must still be reconciled against the traditional view that the distance to the surface is the upper bound of isotropic motions. While other studies have also noted near-surface spectral slopes of −5/3 and have estimated dissipation [*Brumley and Jirka*, 1987; *Chickadel et al.*, 2011], they note that the interpretation is subject to debate both because 2-D turbulence can also produce a −5/3 slope and because Kolmogorov's −5/3 scaling explicitly requires locally isotropic conditions [*Kolmogorov*, 1941].

[55] Several independent observations support the view that the inertial cascade is present in surface boils. First, we note that the −5/3 slope is observed in vertical spectra at 0.02 mbs down to the Nyquist frequency of 12.5 Hz, which corresponds to the 0.05 m scale. Since 2-D turbulence requires a large aspect ratio between horizontal and vertical scales, a −5/3 slope near the 0.05 m scale is most likely due to the turbulent cascade and not 2-D turbulence. The observation that an idealized eddy with diameter 0.05 m centered at 0.02–0.03 mbs would only be mildly affected by blocking effects [see *Troiani et al.*, 2004] supports this inference. Since the −5/3 slope is continuous and self-similar from the 0.05 m scale to the boil scale of 1 m, the inertial cascade is phenomenologically connected between these two scales. The observation that vertical variance is nearly equal to horizontal variance at 1 Hz (Figure 12) also supports the view that a turbulence cascade exists at the boil scale. Finally, ε estimates made at 0.02 mbs using the inertial cascade method are consistent with an approximately linear decrease in water-column dissipation (Figure 8).

[56] For these reasons, an assumption of "approximate isotropy" at the boil scale appears justified. As described earlier, the quality of ADV data was good and the different spectral behavior of vertical and horizontal velocity components at low frequencies (and the good correspondence between Figures 12c and 13) suggests that any alignment issues were minimal. We note, however, that our conclusions are based on only one near-surface measurement and that more complete in situ visualization and measurement of near-surface boils and velocity structure must be made to confirm our results [see also *Nezu and Nakagawa*, 1993].

4. Discussion

[57] We observe that boils are upwelled from lower in the water column (Figures 5 and 7) and dissipate more TKE than ambient flow (Figure 10). Shear and TKE production are largest near the bottom, and produce a nonzero TKE flux-divergence throughout the water column (Figure 8). Moreover, the TKE in the lower half of the water column is more than twice the surface TKE. Therefore, the observation that velocity variance in the most energetic boils (Figure 7) is more than twice the ambient variance suggests that the boils are derived from the lower water column. Further, the observations of ADCP velocity suggest that flow structures extend through the water column (see section 3, supporting information). Though we cannot exclude the possibility that the boils we observe are produced by shear in the upper water column, the evidence suggests that CS are produced in the lower water column near the bed and are an important mechanism for the vertical transport of TKE and the surface TKE balance.

[58] We evaluate more closely the role that CS play in the vertical redistribution of turbulence by evaluating the probability distribution of $-\Phi dw/dz$ during an energetic, 15 min period (Figure 14; equation (9)). Results are segregated into boils (positive IR anomaly) and ambient fluid (negative IR anomaly). Positive values of $-\Phi dw/dz$ denote turbulent energy that is being moved upward from below and spread on the water surface. Similarly, negative values of $-\Phi dw/dz$ denote the convergence of turbulent energy and its subduction into the water column (we presume that this is turbulent energy that was previously upwelled). Figure 7 shows that both boils and ambient fluid exhibit periods of upwelling and downwelling, which result in a $-\Phi dw/dz$ distribution that contains both positive and negative divergence values (Figure 14a). However, both the mean and variance of the two distributions are statistically different. Boils exhibit a positive $\overline{-\Phi dw/dz}$, and are thus moving TKE upward to the water surface as expected. By contrast, $\overline{-\Phi dw/dz}$ is negative in nonboil areas, suggesting that TKE is fluxed downward. Similar distributions are found at other times.

[59] The average TKE transported upward and downward in Figure 14 is not equal, and a residual upward flux divergence of 4.2×10^{-5} m^{2}s^{-3} is found by averaging $\overline{-\Phi dw/dz}$ over 15 min. The result is the same order of magnitude as the surface production, dissipation, and TKE flux divergence estimates (Figures 8 and 14b, and supporting information). Indeed, over a tidal period, the TKE flux divergence estimated by the IR closely follows the transport term estimated from in situ ADVs (Figure 14b).

[60] One implication of Figure 14 is that TKE flux divergence can be estimated using only surface flow features. Second, coherent structures (boils) feed the nonzero TKE flux divergence T_d that is observed throughout the water column. The smaller TKE in the ambient flow ensures that more turbulence is transported upward than downward at the surface (since the mass of upwelling and downwelling fluid must be equal). The finding that CS are responsible for a significant vertical flux of TKE agrees with conclusions from previous laboratory studies [e.g., *Hurther et al.*, 2007]; however, to our knowledge, these are the first observations to confirm this in the field.

[61] Nonetheless, the probability distribution in Figure 14 shows that the balance between upwelling boils and the downwelling ambient flow is subtle (a small difference between two larger numbers), with outliers in the boil distribution responsible for the positive upward flux divergence. The large number of points ($>2 \times 10^5$) used in the analysis increases our confidence in the results (see section 2 for error estimates).

[62] Our results confirm the hypothesis underlying the "chain-saw" model, in which large-scale coherent structures serve to move turbulence to the surface but are filtered away by the surface boundary condition [*Moog and Jirka*, 1999]. Interestingly, we observe that relatively large scales make it to the surface; conglomerations of boils and turbulent motions observed at the surface by the IR are nearly as large as the depth (Figures 4–7). Similarly, velocity fluctuations on the scale of boils (1 m) produce a substantial vertical variance even at 0.02 mbs (Figure 11). Further, we show that energy dissipation is elevated within boils.

Because TKE dissipation controls air-gas transfer [*Moog and Jirka*, 1999; *Zappa et al.*, 2007], this suggests that CS play a significant role in gas exchange. Some blockage of vertical variance is observed to occur at the 5 m "boil patch" scale, as vertical velocity is suppressed (Figure 13). Combined, these observations support the *Moog and Jirka* [1999] hypothesis, provided the boil scale is considered "small".

5. Conclusions

[63] We have used a novel experimental platform to make near-surface and water column turbulence measurements, colocated with thermal imaging of boils on the water surface. Our measurements show that boils are low-momentum water masses with elevated TKE and vertical velocity variance relative to the ambient surface water. These surface CS are marked by horizontal divergence and upwelling, which is caused by the interaction of coherent structures with the kinematic boundary condition. To preserve continuity, downwelling occurs at boil boundaries and in the ambient flow.

[64] The TKE budget in the water column indicates that production and dissipation are not in balance, as is commonly assumed. Instead, production P exceeds dissipation ε near the bottom of the river; this excess shear production exceeds the local capacity to dissipate TKE, causing a local imbalance in the TKE budget. Hence, excess TKE is transported away from the bottom toward the surface where it can be dissipated. Estimates of TKE transport close the $P-\varepsilon$ imbalance in the lower water column and are double the $P-\varepsilon$ imbalance in the mid water column. We expect that the pressure term or the horizontal terms in the TKE equation are required to close the TKE budget, particularly near the surface.

[65] Our observations suggest that CS play an important role in this vertical transport (and dissipation) of TKE and are probably fed by the excess TKE produced near the bottom. On average, between two and three times more TKE dissipation occurs in boils than in the ambient free stream. An upward flux of TKE by CS likely maintains this excess dissipation, and boils brings more TKE to the surface than is transported away from the surface by downwelling from the ambient free stream. Our results hence support the hypotheses of *Moog and Jirka* [1999], which contends that CS preferentially carry elevated TKE and ε to the water surface.

[66] The water surface suppresses vertical motions with a scale greater than the depth H but admits smaller, boil-scale motions. Hence, a marked scale dependence of statistical isotropy develops, with anisotropic conditions observed near the surface for scales greater than the depth H, and approximately equal vertical and horizontal velocity variance observed at scales equal to or smaller than the boil scale of O(1 m). Such statistically isotropic conditions are forced by the spatial structure of the surface, which contains patchy regions of upwelling and downwelling. While this suggests that the observed $-5/3$ dependence of velocity spectra at boil scales is caused by the inertial cascade, more research in needed to corroborate this result.

References

Adrian, R. J., C. D. Meinhart, and C. D. Tomkins (2000), Vortex organization in the outer region of the turbulent boundary layer, *J. Fluid Mech.*, *422*, 1–54.

Bennett, S. J., and J. L. Best (1995), Mean flow and turbulence structure over fixed, two-dimensional dunes: Implications for sediment transport and bedform stability, *Sedimentology*, *42*, 491–513.

Best, J. (2005), The fluid dynamics of river dunes: A review and some future research directions, *J. Geophys. Res.*, *110*, F04S02, doi:10.1029/2004JF000218.

Babakaiff, C. S., and E. J. Hickin (1996), Coherent flow structures in Squamish River Estuary, British Columbia, Canada, in *Coherent Flow Structures in Open Channels*, edited by P. J. Ashworth et al., pp. 321–342, John Wiley, Chichester, U. K.

Brochini, M., and D. H. Peregrine (2001), The dynamics of strong turbulence at free surfaces, Part 1: Description, *J. Fluid Mech.*, *449*, 225–254.

Brumley, B. H., and G. H. Jirka (1987), Near-surface turbulence in a grid stirred tank, *J. Fluid Mech.*, *183*, 253–263.

Chickadel, C. C., A. R. Horner-Devine, S. A. Talke, and A. T. Jessup (2009), Vertical boil propagation from a submerged estuarine sill, *Geophys. Res. Lett.*, *36*, L10601, doi:10.1029/2009GL0372782010.

Chickadel, C. C., S. A. Talke, A. R. Horner-Devine, and A. T. Jessup (2011), Infrared based measurements of velocity, turbulent kinetic energy and dissipation at the water surface in a tidal river, *Geosci. Remote Sens. Lett. 8*(5), p. 849–853.

Coleman, J. M. (1969), Brahmaputra River: Channel processes and sedimentation, *Sediment. Geol.*, *3*, 129–239.

Fairall, C. W., E. F. Bradeley, J. S. Godfrey, G. A. Wick, J. B. Edson, and G. S. Young (1996), Cool-skin and warm-layer effects on sea surface temperature, *J. Geophys. Res.*, *101*, 1295–1308.

George, R., R. E. Flick, and R. T. Guza (1994), Observations of turbulence in the surf zone, *J. Geophys. Res.*, *99*, 801–810.

Giddings, S. N., D. A. Fong, and S. G. Monismith (2011), Role of straining and advection in the intratidal evolution stratification, vertical mixing, and longitudinal dispersion of a shallow, macrotidal, salt wedge estuary, *J. Geophys. Res.*, *116*, C03003, doi:10.1029/2010JC006482.

Hunt, J. C. R. (1984), Turbulence structure in thermal convection and shear-free boundary layers, *J. Fluid Mech.*, *138*, 161–184.

Hurther, D., U. Lemmin, and E. A. Terray (2007), Turbulent transport in the outer region of rough wall open-channel flows: The contribution of Large Coherent Shear Stress Structures (LC3S), *J. Fluid Mech.*, *574*, 465–493.

Jackson, R. G. (1976), Sedimentological and fluid-dynamic implications of the turbulent bursting phenomenon in geophysical flows, *J. Fluid Mech.*, *77*(3), 531–560.

Kadota, A., and I. Nezu (1999), Three dimensional structure of space time correlation on coherent vortices generated behind dune crest, *J. Hydraul. Res.*, *37*, 59–80.

Kolmogorov, A. N. (1941), The local structure of turbulence in incompressible viscous fluid for very large Reynolds number, *Dokl. Akad. Nauk SSSR*, *30*, 299–303.

Kostaschuk, R. A., and M. A. Church (1993), Macroturbulence generated by dunes—Fraser River, Canada, *Sediment. Geol.*, *85*(1–4), 25–37.

Larocque, J., N. Rivière, S. Vincent, D. Reungoat, J. Faure, J. Heliot, J. Caltagirone, and M. Moreau (2009), Macroscopic analysis of a turbulent round liquid jet impinging on an air/water interface in a confined medium, *Phys. Fluids*, *21*, 065110.

Matthes, G. H. (1947), Macroturbulence in natural stream flow, *Eos Trans. AGU*, *28*, 255–265.

Moog, D. B., and G. H. Jirka, (1999), Air-water gas transfer in uniform channel flow, *J. Hydraul.*, *125*, 3–10.

Müller, A., and A. Gyr (1986), On the vortex formation in the mixing layer behind dunes, *J. Hydraul. Res.*, *24*, 359–375.

Nezu, I. (2005), Open-channel flow turbulence and its research prospect in the 21st century, *J. Hydraul. Eng.*, *131*, 229–246.

Nezu, I., and H. Nakagawa (1993), *Turbulence in Open-Channel Flows, IAHR Monogr. Ser.*, A.A. Balkema, Rotterdam, Netherlands.

Nimmo-Smith, W. A. M., S. A. Thorpe, and A. Graham (1999) Surface effects of bottom-generated turbulence in a shallow tidal sea, *Nature*, *400*, 251–254.

Orton, P., C. J. Zappa, and W. R. McGillis (2010), Tidal and atmospheric influences on near surface turbulence in an estuary, *J. Geophys. Res.*, *115*, C12029, doi:10.1029/2010JC006312.

Percival, D. B., and A. T. Walden (1993), *Spectral Analysis for Physical Applications: Multitaper and Conventional Univariate Techniques*, Cambridge Univ. Press, Cambridge, U. K.

Saunders, P. M. (1967), The temperature at the ocean-air interface, *J. Atmos. Sci.*, *24*, 269–273.

Schimpf, U., C. Garbe, and B. Jahne (2004), Investigation of transport processes across the sea surface microlayer by infrared imagery, *J. Geophys. Res.*, *109*, C08S13, doi:10.1029/2003JC00180.

Scully, M. E., W. R. Geyer, and J. H. Trowbridge (2011), The influence of stratification and nonlocal turbulent production on estuarine turbulence: An assessment of turbulence closure with field observations. *J. Phys. Oceanogr.*, *41*, 166–185, doi:10.1175/2010JPO4470.1.

Shen, L., X. Zhang, D. K. P. Yue, and G. Tirantafyllou (1999), The surface layer for free-surface turbulent flows, *J. Fluid Mech.*, *386*, 167–212.

Stacey, M. T. (2003), Estimation of diffusive transport of turbulent kinetic energy from acoustic Doppler current profiler data, *J. Atmos. Oceanic Technol.*, *20*(6), 927–935, doi:10.1175/1520-0426(2003)020<0927: EODTOT>2.0.CO;2.

Stacey, M. T., S. G. Monismith, and J. R. Burau (1999), Measurements of Reynolds stress profiles in unstratified tidal flow, *J. Geophys. Res.*, *104*, 10,933–10,949.

Talke, S. A., A. R. Horner-Devine, and C. C. Chickadel (2010), Mixing layer dynamics in separated flow over an estuarine sill with variable stratification, *J. Geophys. Res.*, *115*, C09004, doi:10.1029/2009JC005467.

Tennekes, H., and J. L. Lumley (1972), *A First Course in Turbulence*, MIT Press, Cambridge, Mass.

Troiani, G., F. Cioffi, and C. M. Casciola (2004), Free-surface–vorticity interactions in an open channel flow, *J. Hydraul. Eng.*, *130*(4), 313–323, doi:10.1061/(ASCE)0733-9429(2004)130:4(313).

Venditti, J. G., and S. J. Bennett (2000), Spectral analysis of turbulent flow and suspended sediment transport over fixed dunes, *J. Geophys. Res.*, *105*, 22,035-22,047, doi:10.1029/2000JC900094.

Wang, B., S. N. Giddings, O. B. Fringer, E. S. Gross, D. A. Fong, and S. G. Monismith (2011), Modeling and understanding turbulent mixing in a macrotidal salt wedge estuary, *J. Geophys. Res.*, *116*, C02036, doi: 10.1029/2010JC006135.

Wiles, P. J., T. P. Rippeth, J. H. Simpson, and P. J. Hendricks (2006), A novel technique for measuring the rate of turbulent dissipation in the marine environment, *Geophys. Res. Lett.*, *33*, L21608, doi:10.1029/2006GL027050.

Yalin, M. S. (1992), *River Mechanics*, Pergamon, Oxford, U. K.

Zappa, C. J., W. R. McGillis, P. A. Raymond, J. B. Edson, E. J. Hintsa, H. J. Zemmelink, J. W. H. Dacey, and D. T. Ho (2007), Environmental turbulent mixing controls on air-water gas exchange in marine and aquatic systems, *Geophys. Res. Lett.*, *34*, L10601, doi:10.1029/2006GL028790.

Zhang, C., L. Shen, and D. K. P. Yue (1999), The mechanism of vortex connection at a free surface, *J. Fluid Mech.*, *384*, 207–241.